Microbubble-Enhanced Focused Ultrasound Improves Targeted Adeno-Associated Virus Delivery in Brain Tumors Quantified by PET Imaging

Yutong Guo[1], Josquin Foiret[1], Jai Woong Seo[1], Nisi Zhang[1], James Wang[1], Marina Nura Raie[1], Basit Latief Jan[1], Spencer K. Tumbale[1], Katherine W. Ferrara[1*]

Affiliations

[1] Molecular Imaging Program at Stanford (MIPS), Department of Radiology, School of Medicine, Stanford University, Stanford, CA, USA.

***Corresponding author**

Katherine W. Ferrara (kwferrar@stanford.edu)

Abstract

Gene therapy using adeno-associated virus (AAV) vectors shows promise for cancer treatment through molecular intervention, yet achieving sufficient and targeted delivery to brain tumors via systemic administration remains limited by the biological barriers. Here, we investigate whether microbubble-enhanced focused ultrasound (MB-FUS) enhances targeted delivery of systemically administered AAV to orthotopic gliomas, using quantitative PET imaging of ^{64}Cu-radiolabeled AAV9 vectors and fluorescent reporter expression to assess biodistribution and functional efficacy. PET imaging at 21 hours post-injection revealed 3.2-fold higher ^{64}Cu-AAV accumulation in MB-FUS-treated tumors compared to non-sonicated tumors (n=3, p=0.004). Quantitative PCR analysis of tumor tissue at the same timepoint confirmed enhanced vector delivery, demonstrating 6.4-fold increased genome copies in MB-FUS-treated tumors (p=0.0003). Optical reporter gene imaging at 17 days post-treatment revealed that enhanced vector delivery translated to significantly increased transgene expression, with 5.3-fold higher transduction in MB-FUS-treated tumors (p=0.0002). These results establish that MB-FUS enables spatially-targeted AAV delivery with quantifiable enhancement of both acute vector biodistribution and downstream transgene expression. The integration of radiolabeled AAV with PET imaging provides a non-invasive methodology for real-time assessment of vector delivery and optimization of treatment protocol for brain cancer gene therapy.

Keywords: Targeted drug delivery; Image-guided delivery; Blood-tumor barrier; Adeno-associated virus; Focused ultrasound; Microbubble; Positron emission tomography; Glioblastoma

Introduction

Despite extensive research and advances in therapy, from multimodal regimens combining surgery, radiotherapy, and chemotherapy to emerging immunotherapies and targeted molecular agents, malignant brain tumors remain among the most devastating cancer diagnoses [1–5]. Glioblastoma (GBM), the most aggressive subtype, has a median survival of only 15 months [6,7]. These treatment strategies, which have shown promise in other cancer types, face formidable obstacles in brain tumors: infiltrative growth that extends beyond resectable margins, intrinsic chemo-radioresistance, immunosuppressive microenvironments, and restrictive biological barriers that limit drug delivery [5,8,9]. Overcoming these barriers requires both novel therapeutic agents and effective delivery strategies.

Gene therapy using adeno-associated viruses (AAVs) represents a promising approach to target multiple mechanisms of treatment resistance [10,11]. By transducing tumor cells and cancer-associated stromal cells, AAVs enable sustained expression of diverse therapeutic payloads, including tumor suppressors[12], pro-apoptotic factors[13,14], anti-angiogenic agents[15–17], and immunostimulatory cytokines[18–22], offering versatility not achievable with conventional therapies. However, realizing the therapeutic potential of AAV gene therapy for brain tumors faces a critical obstacle: achieving

spatially targeted vector delivery across the blood-brain and blood-tumor barriers (BBB/BTB) and adequate penetration and distribution within the tumor microenvironment [23].

Microbubble-enhanced focused ultrasound (MB-FUS) is emerging as a non-invasive tool for overcoming delivery barriers in brain tumors [24,25]. By precisely targeting the tumor regions, MB-FUS transiently increases BBB/BTB permeability and enhances interstitial transport, creating a therapeutic window for enhanced drug delivery [24,26,27]. This approach has been leveraged in completed and ongoing clinical trials to enhance delivery of a variety of therapeutics, including chemotherapeutics and antibodies, to brain tumors, with demonstrated safety and preliminary evidence of efficacy [28]. Despite these promising capabilities and growing clinical application, the potential of MB-FUS to enhance AAV vector delivery and biodistribution in brain tumors has not been investigated. While MB-FUS has been shown to enhance AAV delivery in healthy brain tissue[29–41], the heterogeneous tumor microenvironment may significantly alter vector distribution and transduction efficiency [9]. Furthermore, current assessment methods such as gadolinium-based contrast magnetic resonance imaging (MRI), while useful for confirming BBB opening, do not provide quantitative information on AAV biodistribution or transduction [42]. Quantitative and longitudinal imaging is therefore needed to directly measure AAV biodistribution kinetics with MB-FUS and assess improvements in tumor delivery.

In this work, we investigated whether MB-FUS can enhance spatially targeted AAV delivery to orthotopic GL26 glioma model using quantitative imaging to assess vector biodistribution and transgene expression in vivo. We radiolabeled AAV vectors with ^{64}Cu and encoded a fluorescent reporter gene to enable dual-modality assessment: (1) non-invasive, longitudinal positron emission tomography (PET) imaging to track biodistribution at multiple time points following systemic administration and MB-FUS treatment, and (2) optical imaging to assess biodistribution of transgene expression with fluorescence microscopy for cellular-level analysis. Our approach provides direct, quantitative assessment of both MB-FUS-mediated AAV delivery and functional transduction in brain tumors, establishing a framework for optimizing the treatment protocol to maximize therapeutic effect.

Results

US guided FUS systems for targeted BBB/BTB opening in GL26 glioma tumor.

In this study, we employed an orthotopic GL26 glioma model in which firefly luciferase/eGFP-expressing GL26 cells were stereotactically implanted in B6 Albino mice. To validate that MB-FUS enhances delivery across the BBB/BTB, we first assessed delivery of 70 kDa fluorescently labeled dextran (diameter ~14 nm) to GL26 tumors with and without MB-FUS, administered intravenously 1 minute prior to sonication. MB-FUS was performed two weeks post-implantation using an ultrasound-guided focused ultrasound (USgFUS) system integrating an imaging array (L12-5, Philips/ATL) that enabled precise spatial targeting through real-time visualization of tumor anatomy and co-registration with pre-acquired MRI, and a 1.5-MHz therapeutic transducer (128-element 2D array) (Fig. 1 A-B) [43]. The therapeutic array enabled tumor-specific treatment region design through volumetric raster-scanning, with a 5 × 5 grid (0.5 mm spacing) configured to match tumor volume and achieve full coverage. Sonication was performed concurrently with intravenous MB administration (2.5×10^8 MBs/kg) using the following parameters: 320 kPa peak negative focal pressure, 1 ms pulse duration for each grid point, and 5 Hz pulse repetition frequency of the grid. During treatment, the imaging transducer was used to monitor cavitation dynamics in real-time and provided passive acoustic mapping (PAM) to localize acoustic emissions [44]. This feedback mechanism ensured sonication remained within safety thresholds.

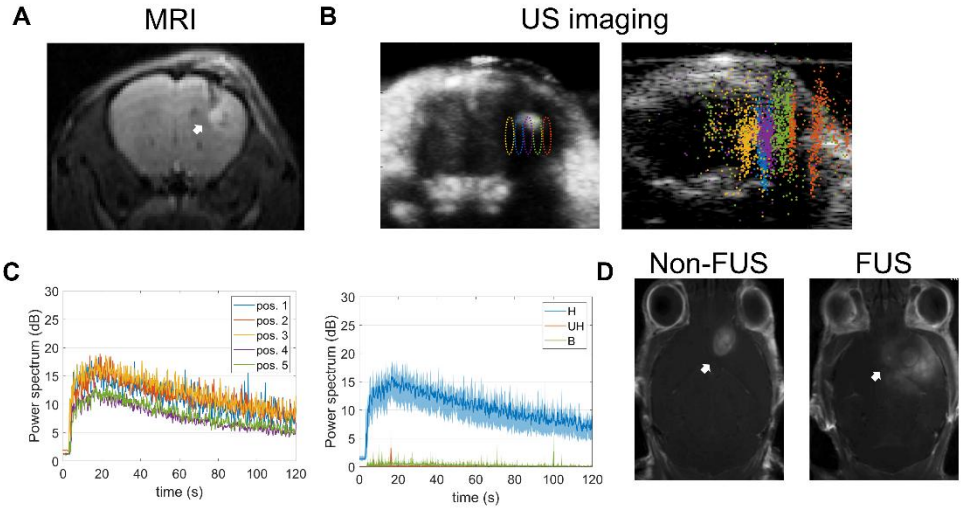

Fig. 1. A) Representative T2 weighted MR image of tumor two weeks after implantation. B) Corresponding maximum intensity projection image from contrast-enhanced ultrasound images after MB administration showing the tumor and FUS target area (left; each colored ellipse indicates a focus location from the treatment grid aligned with the imaging plane). Post-FUS passive acoustic map localizing acoustic emissions from MBs for the entire treatment (right; each colored point cloud corresponds to a focus location and each point to an individual treatment pulse). C) Representative power levels of acoustic emissions originating from MB oscillations during the 120-s treatment. Emissions are processed in the frequency domain in specific bands (H: harmonics, UH: ultra-harmonics, B: broadband). Left: power spectrum as a function of time in the H band for each of the 5 in-plane focus locations. Right: average power spectrum for all 5 focus locations for the H, UH and B frequency bands as a function of time. D) Representative contrast enhanced T1-weighted MR image 10 minutes after MB-FUS treatment (right) or control non-FUS treatment (left). Without FUS, contrast accumulation within the tumor results from the leaky vascular environment (left). After MB-FUS treatment (right), the wider uptake in the tumor area indicates successful BBB opening.

Contrast-enhanced ultrasound imaging following MB administration enabled visualization of tumor morphology and location for confirmation of targeting during treatment (Fig. 1B, Suppl. Fig. 1A). Post-treatment passive acoustic mapping (PAM) analysis revealed spatially localized cavitation events during sonication, validating accurate tumor targeting (Fig. 1C). Additionally, power spectral analysis demonstrated minimal broadband noise throughout treatment, indicating stable MB oscillation without collapse (Fig. 1C, Suppl. Fig. 1B). This is critical for safety, as broadband emissions are associated with MB destruction and potential hemorrhage. To confirm vascular barrier opening, we performed gadolinium-enhanced T1-weighted MRI 10 minutes after sonication. Focal contrast enhancement localized to the sonicated tumor region (Fig. 1D) demonstrated successful BBB/BTB opening with precise spatial targeting.

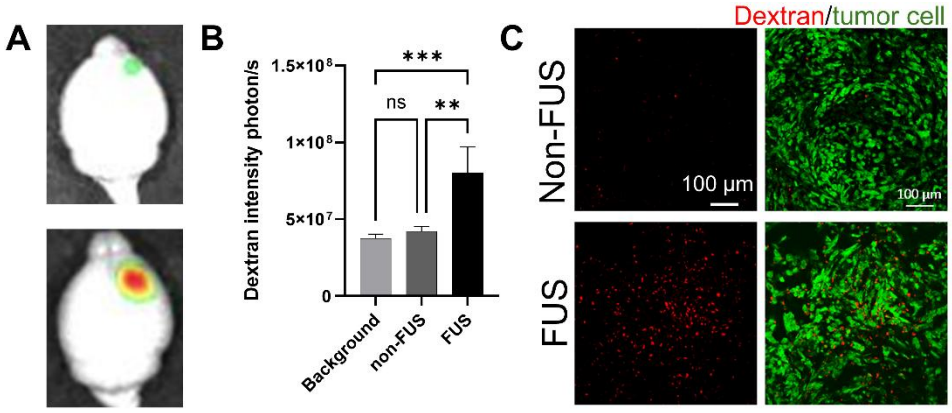

Fig. 2. A) Representative ex vivo images of 70 kDa dextran distribution in the brain 1 hour after treatment. B) Quantification of ex vivo imaging of dextran delivery in the brain 1 hour after treatment. C) Representative confocal microscopy of dextran distribution in the tumor. Red: dextran, green: tumor cells. P-values were determined by two-way analysis of variance (ANOVA) and were adjusted using Bonferroni correction. Plots show mean ± S.D (n=5). **P ⩽ 0.01, ***P ⩽ 0.001.

Importantly, ex vivo fluorescence imaging confirmed enhanced dextran delivery 1 hour following MB-FUS treatment. Whole-brain imaging showed localized dextran accumulation at the sonicated tumors, with quantification revealing a 2-fold increase compared to untreated contralateral tumors (p=0.0015) (Fig. 2A). Microscopic analysis demonstrated substantially greater dextran accumulation throughout MB-FUS-treated tumors compared to non-FUS treated tumors (Fig. 2B). Together, these data demonstrate that MB-FUS enhances delivery of macromolecular therapeutics to orthotopic gliomas in immunocompetent mice.

Longitudinal PET imaging of ^{64}Cu-labeled AAV9 demonstrates MB-FUS-mediated enhancement of vector delivery in GL26 glioma tumor.

Having established that MB-FUS enhances macromolecular delivery to brain tumors, we next quantitatively assessed MB-FUS-mediated enhancement of AAV vector delivery in orthotopic gliomas using PET imaging of ^{64}Cu-labeled AAVs. AAV9 was selected due to its well-established systemic biodistribution profile and tropism for brain tissue [29,45]. Tumor growth was monitored by MRI and bioluminescence imaging, and mice were assigned to treatment groups based on tumor volume to ensure comparable microenvironmental characteristics across groups (Fig. 3A, Suppl. Fig. 2). Two weeks post-implantation, ^{64}Cu-labeled AAV9 (1×10^{13} vg/kg, 5-8 μCi/mouse) was administered intravenously immediately prior to MB-FUS treatment, following the protocol established for dextran. Real-time ultrasound imaging confirmed tumor localization (Fig. 3B), while passive acoustic monitoring demonstrated stable microbubble oscillations throughout treatment within the safety regime (Fig. 3C).

To track AAV biodistribution dynamics, we performed longitudinal PET imaging at 0.5, 6, and 21 hours post-treatment. PET imaging at all timepoints showed localized radiolabeled capsid accumulation in the MB-FUS-treated tumors, demonstrating both enhancement and spatial specificity of delivery (Fig. 3D). At the earliest timepoint (0.5 h), elevated ^{64}Cu signal was observed in tumor regions in both groups, likely reflecting circulating AAVs in the vasculature. However, by 21 hours, as circulating AAVs cleared, the most pronounced differential accumulation was observed, with quantitative analysis revealing a 3.2-fold increase in ^{64}Cu activity in MB-FUS-treated tumors compared to non-FUS treated tumors (n=3, p=0.004, Fig. 3E). To corroborate PET imaging findings, we quantified AAV9 genome copies in tumor tissue at 21 hours using quantitative polymerase chain reaction (qPCR). Biodistribution analysis revealed a 6.4-fold increase in vector genome copies in MB-FUS-treated tumors compared to non-treated contralateral tumors (n=5, p=0.0003, Fig. 3F), confirming the PET imaging quantification.

Together, these data demonstrate that MB-FUS significantly enhances spatially targeted AAV9 delivery to orthotopic gliomas with sustained vector retention. Moreover, quantitative ^{64}Cu-PET imaging provides non-invasive assessment of AAV biodistribution and pharmacokinetic insights that can inform optimization of treatment timing and treatment parameters for future therapeutic applications.

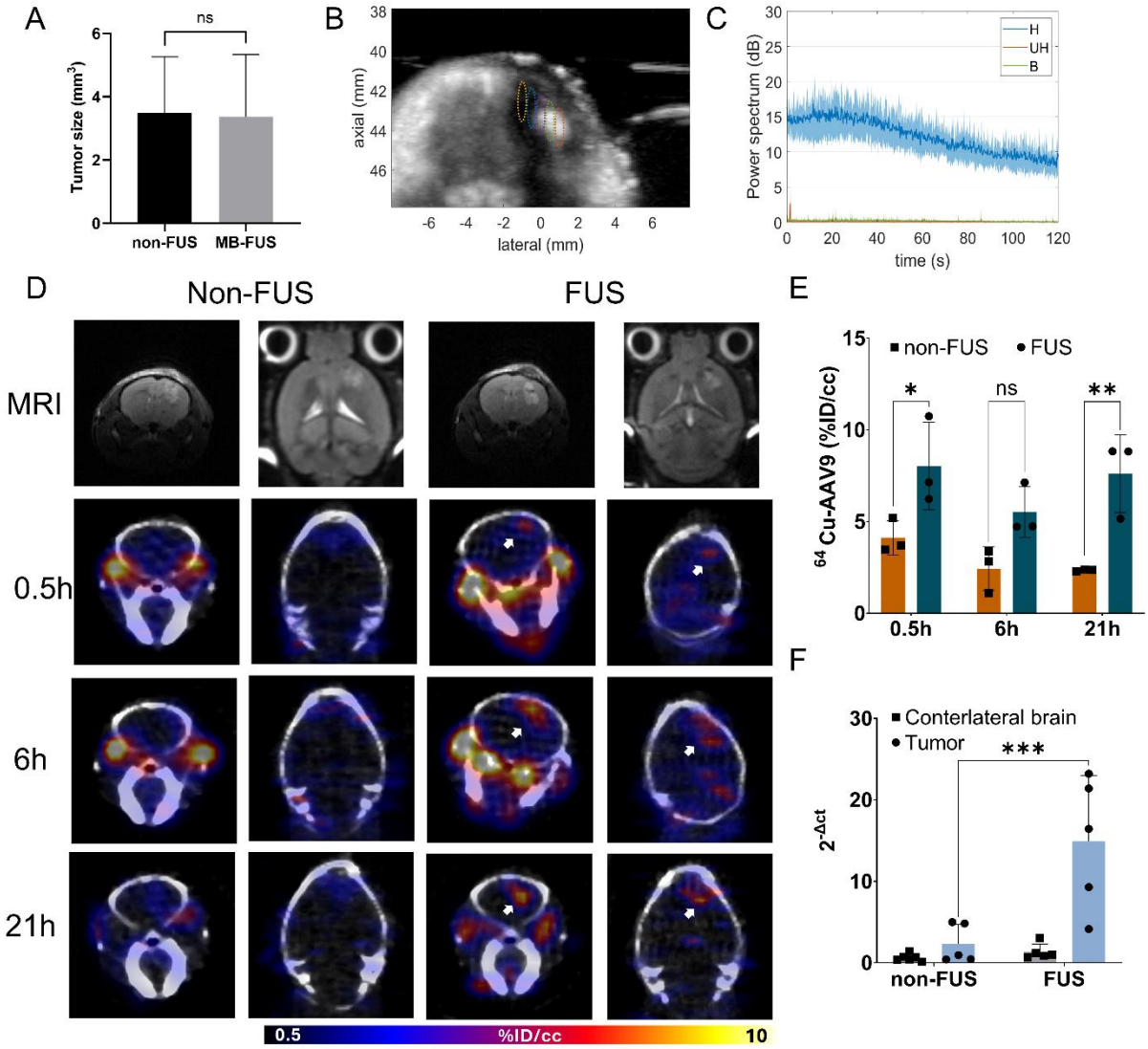

Fig. 3. A) Tumor size quantification with T2 weighted MRI showing comparable volumes between non-FUS and MB-FUS treatment groups prior to treatment. B) Representative MB contrast-enhanced ultrasound image with overlaid treatment grid (colored dotted lines) confirming tumor localization for targeted sonication. C) Representative power levels of acoustic emissions originating from MB oscillations during the 120-s treatment. Emissions are processed in the frequency domain in specific bands (H: harmonics, UH: ultra-harmonics, B: broadband). D) Representative T2-weighted MRI (top rows, acquired pre-treatment) and corresponding longitudinal PET images from the same mouse at 0.5, 6, and 21 hours post-treatment for non-FUS control (left) and MB-FUS-treated (right) mice. White asterisks indicate tumor locations. E) Quantification of PET images in tumor regions at 0.5, 6, and 21 hours post-treatment (%ID/cc). P-values were determined by two-way analysis of variance (ANOVA) and were adjusted using Bonferroni correction. (**P ⩽ 0.01) F) Tumor-to-contralateral brain ratio at 21 hours demonstrating enhanced and spatially specific AAV9 delivery to MB-FUS-treated tumors (n= 5, ***p<0.001; unpaired t-test). Data shown as mean ± SD.

Enhanced AAV delivery with MB-FUS resulted in higher transduction efficiency in GL26 glioma tumor.

To assess whether enhanced AAV delivery can lead to functional transgene expression, we administered AAV9 encoding the tdTomato fluorescent reporter and evaluated transduction efficiency in tumors. Given the aggressive growth of the GL26 tumors and the timeline for AAV transduction (peak expression at approximately 1-month post-administration), we modified the treatment protocol to perform treatment 3 days post tumor implantation, providing a sufficient window to monitor transgene expression before animals reached endpoint.

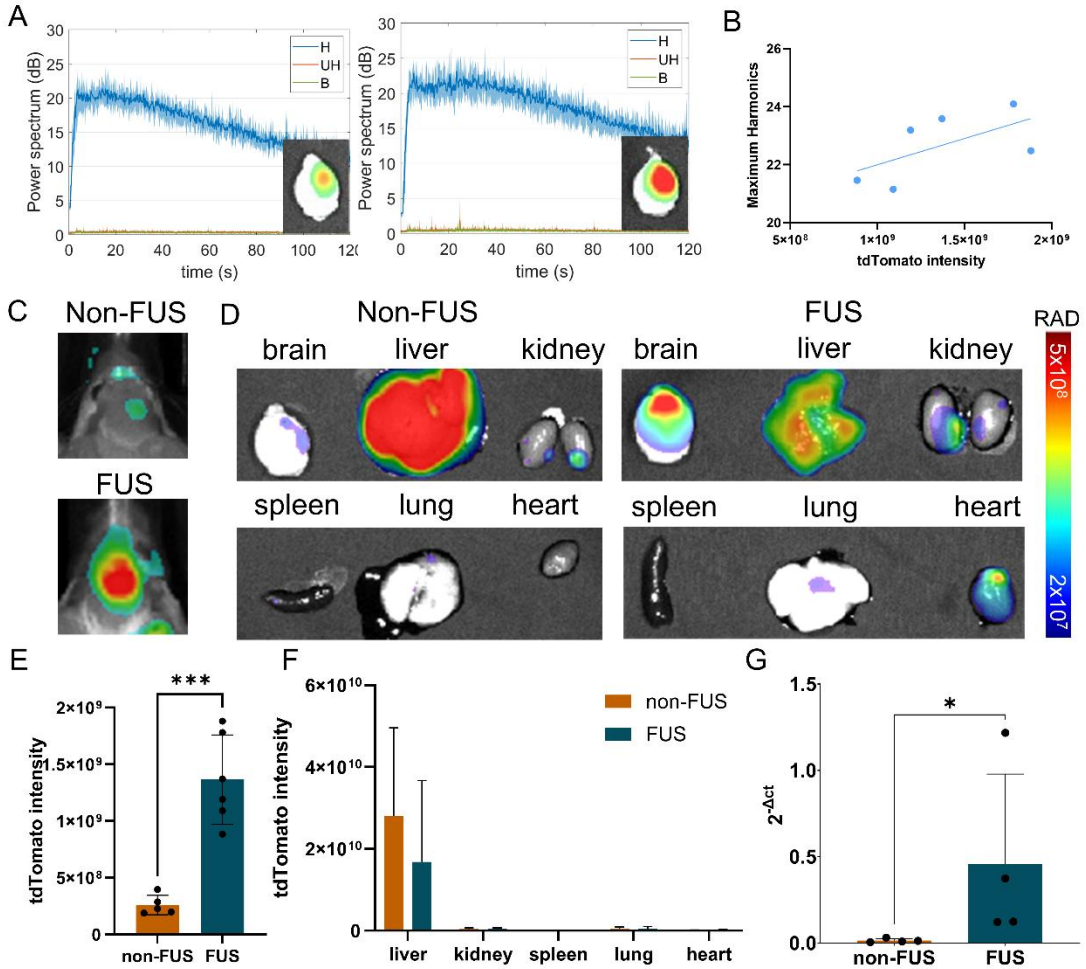

Fig. 4. A) Representative acoustic emission spectra during treatment (H: harmonics; UH: ultraharmonics; B: broadband) with endpoint bioluminescence images (insets). B) Correlation between harmonic levels and tdTomato expression. C) Representative in vivo tdTomato fluorescence at 14 days post-treatment. (D) Ex vivo organ biodistribution showing AAV9 tropism for non-FUS AAV9 only (left) and MB-FUS group (right). E) Quantification of ex vivo tdTomato intensity in the brain tumor region (n=5-6, ***p=0.0002). F) Peripheral organ fluorescence quantification. G) qPCR validation of tumor transgene expression (n=4, *p<0.05). Data: mean ± SD. P-values were determined by unpaired student t-test.

Real-time passive acoustic monitoring during treatment revealed strong harmonic emissions with minimal broadband emissions throughout the 120-second sonication period (Fig. 4A), consistent with safe cavitation dynamics observed in previous experiments. Notably, we observed a positive correlation between harmonic emission levels and subsequent tdTomato expression intensity (Fig. 4A-B, Suppl. Fig.3), suggesting that acoustic monitoring can serve as a real-time predictor of treatment effectiveness and transduction outcomes.

At 17 days post-treatment, in vivo optical imaging revealed robust tdTomato expression localized to the MB-FUS-treated tumor region (Fig. 4C). Ex vivo quantitative analysis demonstrated a 5.3-fold increase in tdTomato fluorescence intensity in MB-FUS-treated tumors compared to non-FUS-treated tumors (p=0.0002, Fig. 4E), demonstrating that enhanced AAV delivery translates to significantly increased transgene expression. Biodistribution analysis of major organs showed expected AAV9 tropism, with high expression in the liver for both groups (Fig. 4D). Interestingly, a trend toward reduced hepatic tdTomato expression was observed in MB-FUS-treated mice, although not statistically significant (Fig. 4F), potentially reflecting more efficient brain retention of systemically administered AAV. qPCR quantification of tdTomato mRNA levels in tumor tissue corroborated the optical imaging findings, demonstrating significantly elevated transgene expression in MB-FUS-treated tumors (Fig. 4G, p<0.05).

To examine the spatial distribution and cellular localization of AAV transduction within the tumor microenvironment, we performed fluorescence microscopy on tumor tissue sections at 17 days post-treatment. In non-FUS-treated tumors, minimal tdTomato-positive cells were observed, with only sparse transduction events within the tumor (Fig. 5, top row). In contrast, MB-FUS-treated tumors demonstrated substantially higher tdTomato expression, with widespread transduction throughout the tumor tissue (Fig. 5, bottom row). Notably, tdTomato signal colocalized with eGFP-positive tumor cells in the merged images, confirming successful transduction of tumor cells.

Collectively, these data demonstrate that MB-FUS-mediated enhancement of AAV delivery results in robust, spatially targeted transgene expression in orthotopic GL26 gliomas. The correlation between acoustic emissions and transduction efficiency suggests that real-time passive acoustic monitoring may enable prediction and optimization of treatment outcomes during sonication.

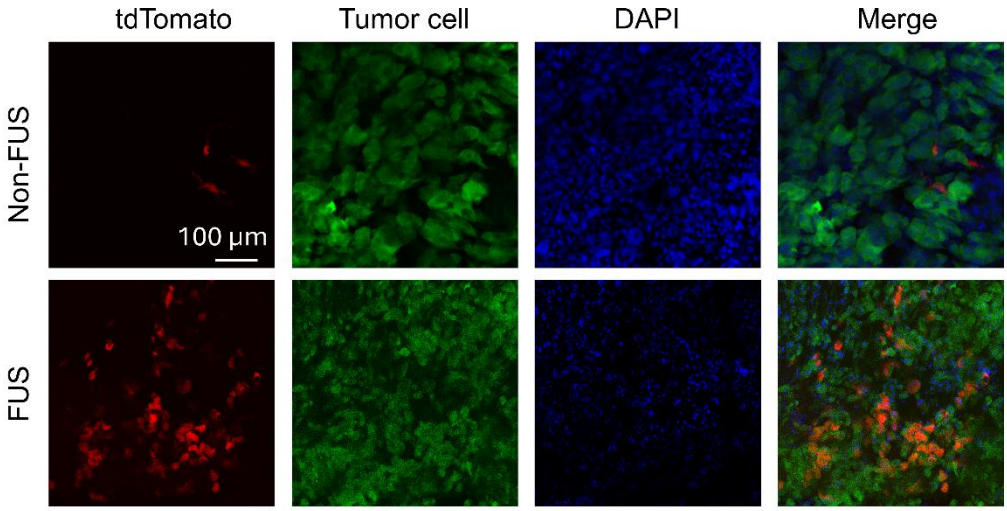

Fig. 5. Representative fluorescence microscopy of tumor sections at 14 days post-treatment. Red: tdTomato (AAV transgene); Green: eGFP (tumor cells); Blue: DAPI (nuclei); Merge: overlay showing colocalization. Non-FUS control (top) shows minimal transduction, while MB-FUS-treated tumor (bottom) demonstrates extensive tdTomato expression throughout tumor tissue with substantial tumor cell colocalization. Scale bar: 100 µm.

Discussion

In this study, we demonstrate that microbubble-enhanced focused ultrasound (MB-FUS) significantly enhances systemic AAV delivery to orthotopic GL26 gliomas and that quantitative PET imaging of radiolabeled AAV provides a method to gauge the vector biodistribution, yielding critical pharmacokinetic insights for optimizing treatment protocols. Using an ultrasound-guided FUS platform integrated with real-time acoustic monitoring, we achieved spatially precise AAV delivery that translated to robust transgene expression in the sonicated tumor regions. These findings establish MB-FUS as a promising non-invasive strategy to overcome BBB/BTB limitations for AAV-mediated gene therapy in brain cancers.

A key advance of this work is the demonstration that MB-FUS can enhance AAV delivery to brain tumors and the use of quantitative PET imaging to provide absolute measurements of AAV biodistribution following MB-FUS treatment. Previous studies have primarily relied on indirect measures of BBB disruption, such as gadolinium-enhanced MRI, which confirm barrier opening but do not quantify therapeutic agent delivery. While gadolinium extravasation demonstrates successful BBB modulation, the pharmacokinetics of large biologics such as AAV vectors differ substantially from small contrast agents [42]. Our ^{64}Cu-PET imaging approach directly measures AAV biodistribution in absolute units (%ID/cc)[43,46], revealing not only enhanced delivery (3.2-fold

increase at 21 hours) but also providing temporal pharmacokinetic data on delivery kinetics and retention. The longitudinal imaging demonstrated that while both tumor regions showed elevated signal at early timepoints due to circulating AAVs, the differential signal between MB-FUS-treated and non-treated tumors became increasingly pronounced over time, indicating both enhanced initial extravasation and sustained retention in sonicated regions. This quantitative pharmacokinetic information is critical for rational optimization of treatment parameters, including optimal timing between AAV administration and sonication, sonication duration, and combination strategies with other therapies.

The ultrasound-guided FUS platform employed in this study enabled precise spatial targeting through real-time visualization of tumor anatomy. The phased-array transducer enables electronic beam steering, allowing tumor-specific treatment grid design, a capability critical for clinical translation, where patient-specific tumor morphology and location require customized treatment planning. Beyond spatial targeting, passive acoustic mapping (PAM) throughout treatment provided real-time feedback on microbubble cavitation dynamics, ensuring robust treatment while remaining within safety limits. Notably, we observed a positive correlation between harmonic emission levels during treatment and subsequent transgene expression, suggesting that acoustic parameters may serve as predictive metrics for treatment efficacy and enable adaptive protocols that optimize outcomes in real-time. Integration of acoustic monitoring with previously demonstrated closed-loop control systems[47–49], could be extended to optimize AAV gene therapy delivery through further investigation of acoustic-transduction relationships.

Critically, we demonstrated that MB-FUS-enhanced AAV delivery translates to robust functional transgene expression, with 5.3-fold increased transduction in treated tumors. Microscopic analysis revealed widespread tdTomato expression throughout the tumor parenchyma with colocalization in tumor cells, confirming efficient AAV penetration beyond the perivascular space into the tumor microenvironment. While this study employed tdTomato as a reporter, the platform is readily translatable to therapeutic transgenes targeting glioma treatment resistance, including immunomodulatory genes (IL-12, IFN-β), tumor suppressors (p53, PTEN), pro-apoptotic factors (TRAIL), and anti-angiogenic agents. Furthermore, recent advances in capsid engineering have generated AAV variants with enhanced tumor tropism [50–53]. Combining these tumor-targeted capsids with MB-FUS could yield synergistic improvements in both delivery efficiency and cellular specificity.

This study establishes MB-FUS as an effective strategy to enhance AAV delivery to brain tumors and demonstrates that quantitative PET imaging enables treatment monitoring and optimization. This integrated platform, combining targeted delivery, predictive acoustic monitoring, and pharmacokinetic quantification, provides essential tools for developing optimized gene therapies for brain malignancies.

Methods

In vivo experiments

All animal experiments were conducted with a protocol approved by the Institutional Animal Care & Use Committee (IACUC) at Stanford University. 2-3 months old B6 albino female mice were used in this study (Jackson Laboratory).

Gl26 glioma cells and tumor inoculation

The murine glioma cell line GL26, genetically modified to express firefly luciferase and eGFP, was provided by Dr. Edwin Chang at Stanford University. GL26 glioma cells were cultured in DMEM media with 10% FBS, 1% Penicillin-Streptomycin (Gibco). 10^5 GL26 cells were stereotactically implanted into the brain at 1 mm anterior and 1 mm to the right of the Bregma of 2 month-old mice.

After cell implantation, tumor growth was monitored using bioluminescence imaging and T2 weighted Magnetic Resonance Imaging (MRI) (Pharmascan 7T, Bruker). To minimize differences in baseline BBB permeability across experimental groups due to tumor size variability, mice were stratified by tumor volume and evenly distributed between control and MB-FUS-treated groups before treatment.

Microbubble preparation and characterization

The MBs used in this study were lipid-shelled MBs produced in-house (distearoylphosphatidylcholine (DSPC):1,2distearoyl-sn-glycero-3-phosphoethanolamine-N-[maleimide(polyethylene glycol)-2000 (DSPE-PEG2000); 90:10 molecular ratio). To independently assess the impact of ultrasound frequency on the bioeffect and to ensure robust and consistent BBB opening, we utilized monodisperse MBs with a 5-µm diameter. These MBs were isolated through size-selective centrifugation of freshly activated polydisperse solution. To make sure the MB sizes and number of MBs selected were consistent using this method, the selected MB were counted and characterized by AccuSizer 770A Optical Particle Sizer (Santa Barbara, CA, USA) in triplicates before every MB-FUS treatment.

Focused Ultrasound System and Treatment

We employed an ultrasound-guided focused ultrasound (USgFUS) system (1.5 MHz) featuring a 128-element 2D therapeutic array integrated with an L12-5 imaging transducer (Philips/ATL), as previously described.[43] A Verasonics Vantage 256 system controlled image guidance, therapy delivery, and acoustic monitoring. The therapeutic transducer was calibrated transcranially using a needle hydrophone (HNP0400, Onda) with age-matched mouse skulls positioned to simulate tumor targeting geometry (focal depth ~4 mm). To ensure complete tumor coverage, the focal zone was raster-scanned across a 5 × 5 grid with 0.5 mm non-overlapping spacing.

Tumor-bearing mice were anesthetized and positioned supine with stereotaxic head fixation. Tumors were localized using real-time ultrasound imaging confirmed with pre-acquired MRI. AAV vectors or fluorescently labeled dextran were administered intravenously 1 minute before sonication. Treatment parameters were: 1 ms pulses, 5 Hz repetition rate, 320 kPa peak negative focal pressure, 2 minutes total duration, with concurrent intravenous microbubble administration (2.5×10^8 MBs/kg). Real-time passive acoustic mapping (PAM) via the imaging transducer was employed to localize acoustic emissions and characterize microbubble cavitation dynamics throughout sonication.[54]

Magnetic resonance imaging

MRI was performed using a Bruker 11.7 Tesla small animal scanner (Bruker BioSpin MRI, Ettlingen, Germany) equipped with a cross coil configuration with a mouse body resonator for transmission and a mouse surface coil for reception. Images were acquired using ParaVision 360 (Bruker BioSpin MRI). Tumor size was assessed using a T2 weighted MRI sequence (2D FLASH sequence, flip angle (FA) = 15°, repetition time (TR) 250 ms, echo time (TE) 15 ms, 1 mm slice thickness, 1 mm interslice distance, 13 images, field of view (FOV) = 2 x 2 cm2, matrix = 192 x 192, number of acquisitions (NA) = 4). To confirm the BBB opening, immediately after the sonication, the animals were injected with the gadolinium contrast agent, Gd-HPDO3A (Prohance®, 0.5 µmol/g mouse body weight). Permeability of the BBB was determined with a T1 weighted (T1w) sequence (2D RARE sequence, RARE factor = 2, repetition time (TR) 250 ms, echo time (TE) 6.7 ms, 1 mm slice thickness, 1 mm interslice distance, 13 images, field of view (FOV) = 2 x 2 cm, matrix = 384 x 384, number of acquisitions (NA) = 6).

Fluorescent optical imaging

Tumor growth, dextran delivery, and transgene expression were monitored using the LAGO imaging system (Spectral Instruments Imaging, Tucson, AZ). For bioluminescence imaging of Fluc-expressing GL26 tumors, mice received intraperitoneal D-luciferin (150 mg/kg) and were imaged 10 minutes later with 2-second exposure. For fluorescence imaging, the appropriate filter sets were used: excitation: 535 nm, emission: 589 nm. Both in vivo and ex vivo fluorescence images were acquired with 2-second exposure. Regions of interest (ROIs) were drawn over tumors or organs, and signal was quantified as total flux (photons/second) for bioluminescence or radiance/total emission for fluorescence using Aura software (Spectral Instruments).

AAV production

AAV9 vectors were produced by the UNC Vector Core (University of North Carolina). Briefly, AAVs were harvested 5 days after triple transfection in HEK293 cells by PEG precipitation of 3- and 5-days media and osmotic lysis of cell pellets. Crude AAVs were then purified by extraction from iodixanol density gradients and buffer exchanged into Dulbecco's phosphate-buffered saline (DPBS). Viral titers were determined by qPCR on a woodchuck hepatitis virus post-transcriptional regulatory element (WPRE) present in all packaged AAV genomes.

Radiolabeling of AAV

All radiolabeling experiments were conducted under the Controlled Radiation Authorization (CRA) approved by Stanford University (Palo Alto, CA). Radiolabeling of AAVs was performed using our previously reported method.[43,46] [^{64}Cu]CuCl2 was produced at the MIR Cyclotron Facility at Washington University School of Medicine. The stock solution of AAV9 (4×10^{12} vg) in PBS (0.2 mL) was mixed with aqueous Na2CO3 (0.1 M, 20 µL, pH = 9.2), 2 mM tetrazine-PEG5-NHS (Tz-PEG5-NHS, 2 nmol, 1 µL in DMSO) and incubated at 25ºC for 30 minutes. After addition of PBS (0.1 mL), the mixture was transferred to a mini-dialysis device (20 kDa molecular weight cut-off (MWCO)), dialyzed in PBS (15 mL) for 4 hours and subsequently transferred for overnight dialysis (500 mL). Dialyzed Tz-AAVs were collected and further incubated over a period of 0.5-1 hours with ^{64}Cu-(NOTA)8-TCO. The latter was freshly prepared from the reaction of [^{64}Cu]CuCl2 (111-148 MBq (3-4 mCi), 4-5 µL) and 10 µM (NOTA)8-TCO (40-100 pmol, 4-10 µL) in ammonium citrate buffer (20 µL, pH 6.5) at room temperature. The incorporation of ^{64}Cu to (NOTA)8-TCO was complete after 30 minutes as monitored by instant thin-layer chromatography (iTLC). After radiolabeling, EDTA (0.5 M, 3 µL) was added to the mixture and allowed to react for a further 15 minutes. Radiolabeled AAVs were purified employing a 100 kDa MWCO centrifugal filter unit (Thermo Fisher Scientific) with PBS (3x15 mL) containing 0.001% Pluronic F-68 (Gibco) and concentrated in a ~200 µL volume.

PET imaging

Longitudinal PET/CT imaging was performed at 0.5, 6, and 21 hours post-treatment using an Inveon microPET/CT scanner (Siemens Medical Solutions). Mice were anesthetized with isoflurane (1-2% in oxygen) and positioned prone with the head centered in the field of view. Static PET acquisitions were performed for 30 minutes per timepoint, followed by CT imaging for anatomical co-registration.

PET data were reconstructed using 3D ordered-subset expectation maximization with maximum a posteriori (3D-OSEM/MAP) algorithm and corrected for decay, dead time, and scatter. PET and CT images were co-registered using Inveon Research Workplace (IRW) software (Siemens). Regions of interest (ROIs) were manually drawn over MB-FUS-treated tumors, contralateral non-treated tumors. Activity concentration was quantified as percent injected dose per cubic centimeter (%ID/cc). For longitudinal comparison, values were decay-corrected to the time of injection.

DNA extraction

To assess AAV9 vector biodistribution, mice were euthanized 21 hours post-treatment, and brains were extracted and bisected into sonicated and non-sonicated hemispheres on ice. The brain sample was immediately stabilized in Allprotect Tissue Reagent (Qiagen) until processing. DNA was isolated from tissue homogenates using the DNeasy Blood & Tissue Kit (Qiagen) according to the manufacturer's protocol. DNA concentration and purity were determined by NanoDrop spectrophotometry (Thermo Fisher Scientific), and samples were diluted to a uniform concentration for qPCR analysis.

RNA extraction and cDNA synthesis

To assess transgene expression, brain tissue was collected and immediately stabilized in RNA-protect tissue reagent (Qiagen) on ice. Total RNA was extracted from brain hemispheres using the RNeasy Midi Kit (Qiagen) following the manufacturer's instructions. During this process, genomic DNA was removed by DNase. RNA integrity and concentration were assessed by NanoDrop spectrophotometry, and samples with an A260/A280 ratio between 1.8 and 2.0 were used for downstream analysis. Complementary DNA (cDNA) was synthesized from 500 ng-1 µg of total RNA using SuperScript IV VILO Master mix (ThermoFisher Scientific) according to the manufacturer's protocol.

Quantitative PCR (qPCR)

qPCR was performed using TaqMan-based assays with primers and probe designed to detect specific genome copies (tdTomato, PKM2, hBDNF, Syn1, Syp, and Dlg4) and normalized to the housekeeping gene, β-actin. Relative expression was calculated using the ΔΔCt method and expressed as fold-change relative to control groups. All reactions were performed in triplicate on a CFX96 (Bio-Rad) system using the following cycling conditions: 95°C for 10 min, followed by 40 cycles of 95°C for 15 s and 60°C for 1 min.

Immunofluorescence staining and microscopy

For protein expression analysis, after the animals were euthanized at the time point based on their treatment protocols, the brains were harvested and were fixed with 4% paraformaldehyde overnight at 4°C. The next day, 20 µm sections were cut using a microtome (Leica 3050 S Cryostat). The sections were imaged with a 20x objective using a fluorescence confocal microscope (Leica DMi8 Inverted Microscope). The quantification of the fluorescence images was performed using ImageJ.

Statistical analysis

All statistical analyses were performed using GraphPad Prism. P values $P < 0.05$ was considered statistically significant. (n.s. no significance, * $P \leq 0.05$, ** $P \leq 0.01$, ** $P \leq 0.001$, ****$P \leq 0.0001$). In the case of multiple comparisons, the p-values were adjusted using Bonferroni correction.

Data availability: All data supporting the findings of this study are available within the article and its supplementary files. Any additional requests for information can be directed to, and will be fulfilled by, the corresponding authors.

Acknowledgments: We thank Dr. Frezghi Habte, Dr. Edwin Chang, and Laura Jean Pisani at the Stanford Center for Innovation in In Vivo Imaging (SCi3) for technical support with PET/CT, optical imaging, and MRI studies. This study was supported by NIH grants R01 CA112356, R01 EB028646 and the Focused Ultrasound Foundation. Y.G. was partially supported by the Focused Ultrasound Foundation Lockhart Postdoctoral Fellowship.

Author contributions: Y.G. and K.W.F. designed research; Y.G, J.F., and N.Z. performed FUS treatment; J.W.S. performed AAV radio labeling; Y.G, N.Z., J.W.S., J.W., and B.L.J. performed PET/CT imaging; Y.G, B.L.J. and M.N.R. inoculated tumors; Y.G.; S.K.T cultured tumor cells; Y.G. and S.K.T performed the bioassay and analyzed the data, B.L.J. and M.N.R. performed animal

care, Y.G. and K.W.F. wrote the manuscript. All authors reviewed the manuscript and approved the final version.

Competing interests: The authors declare that they have no competing interests.

References

1. van Solinge, T. S., Nieland, L., Chiocca, E. A. & Broekman, M. L. D. Advances in local therapy for glioblastoma — taking the fight to the tumour. *Nat Rev Neurol* **18**, 221–236 (2022).
2. Sampson, J. H., Gunn, M. D., Fecci, P. E. & Ashley, D. M. Brain immunology and immunotherapy in brain tumours. *Nat Rev Cancer* **20**, 12–25 (2020).
3. Cioffi, G., Waite, K. A., Edelson, J. L., Kruchko, C., Ostrom, Q. T. & Barnholtz-Sloan, J. S. Changes in survival over time for primary brain and other CNS tumors in the United States, 2004–2017. *J Neurooncol* **160**, 209–219 (2022).
4. Ale, Y. & Nainwal, N. Progress and Challenges in the Diagnosis and Treatment of Brain Cancer Using Nanotechnology. *Mol. Pharmaceutics* **20**, 4893–4921 (2023).
5. Weller, M., Wen, P. Y., Chang, S. M., Dirven, L., Lim, M., Monje, M. & Reifenberger, G. Glioma. *Nat Rev Dis Primers* **10**, 33 (2024).
6. Miller, K. D., Ostrom, Q. T., Kruchko, C., Patil, N., Tihan, T., Cioffi, G., Fuchs, H. E., Waite, K. A., Jemal, A., Siegel, R. L. & Barnholtz-Sloan, J. S. Brain and other central nervous system tumor statistics, 2021. *CA: A Cancer Journal for Clinicians* **71**, 381–406 (2021).
7. Vaz-Salgado, M. A., Villamayor, M., Albarrán, V., Alía, V., Sotoca, P., Chamorro, J., Rosero, D., Barrill, A. M., Martín, M., Fernandez, E., Gutierrez, J. A., Rojas-Medina, L. M. & Ley, L. Recurrent Glioblastoma: A Review of the Treatment Options. *Cancers* **15**, 4279 (2023).
8. Lim, M., Xia, Y., Bettegowda, C. & Weller, M. Current state of immunotherapy for glioblastoma. *Nat Rev Clin Oncol* **15**, 422–442 (2018).
9. Arvanitis, C. D., Ferraro, G. B. & Jain, R. K. The blood–brain barrier and blood–tumour barrier in brain tumours and metastases. *Nat Rev Cancer* **20**, 26–41 (2020).
10. Xu, X., Chen, W., Zhu, W., Chen, J., Ma, B., Ding, J., Wang, Z., Li, Y., Wang, Y. & Zhang, X. Adeno-associated virus (AAV)-based gene therapy for glioblastoma. *Cancer Cell International* **21**, 76 (2021).

405 11. Hacker, U. T., Bentler, M., Kaniowska, D., Morgan, M. & Büning, H. Towards Clinical Implementation
406 of Adeno-Associated Virus (AAV) Vectors for Cancer Gene Therapy: Current Status and Future
407 Perspectives. *Cancers (Basel)* **12**, 1889 (2020).
408 12. Zhong, X., Zhao, H., Liang, S., Zhou, D., Zhang, W. & Yuan, L. Gene delivery of apoptin-derived peptide
409 using an adeno-associated virus vector inhibits glioma and prolongs animal survival. *Biochem Biophys*
410 *Res Commun* **482**, 506–513 (2017).
411 13. Ma, H.-I., Hueng, D.-Y., Shui, H.-A., Han, J.-M., Wang, C.-H., Lai, Y.-H., Cheng, S.-Y., Xiao, X., Chen, M.-
412 T. & Yang, Y.-P. Intratumoral decorin gene delivery by AAV vector inhibits brain glioblastomas and
413 prolongs survival of animals by inducing cell differentiation. *Int J Mol Sci* **15**, 4393–4414 (2014).
414 14. Crommentuijn, M. H., Kantar, R., Noske, D. P., Vandertop, W. P., Badr, C. E., Würdinger, T., Maguire,
415 C. A. & Tannous, B. A. Systemically administered AAV9-sTRAIL combats invasive glioblastoma in a
416 patient-derived orthotopic xenograft model. *Molecular Therapy - Oncolytics* **3**, (2016).
417 15. Harding, T. C., Lalani, A. S., Roberts, B. N., Yendluri, S., Luan, B., Koprivnikar, K. E., Gonzalez-Edick, M.,
418 Huan-Tu, G., Musterer, R., VanRoey, M. J., Ozawa, T., LeCouter, R. A., Deen, D., Dickinson, P. J. &
419 Jooss, K. AAV serotype 8-mediated gene delivery of a soluble VEGF receptor to the CNS for the
420 treatment of glioblastoma. *Mol Ther* **13**, 956–966 (2006).
421 16. Hicks, M. J., Funato, K., Wang, L., Aronowitz, E., Dyke, J. P., Ballon, D. J., Havlicek, D. F., Frenk, E. Z.,
422 De, B. P., Chiuchiolo, M. J., Sondhi, D., Hackett, N. R., Kaminsky, S. M., Tabar, V. & Crystal, R. G.
423 Genetic modification of neurons to express bevacizumab for local anti-angiogenesis treatment of
424 glioblastoma. *Cancer Gene Ther* **22**, 1–8 (2015).
425 17. Yanamandra, N., Kondraganti, S., Gondi, C. S., Gujrati, M., Olivero, W. C., Dinh, D. H. & Rao, J. S.
426 Recombinant adeno-associated virus (rAAV) expressing TFPI-2 inhibits invasion, angiogenesis and
427 tumor growth in a human glioblastoma cell line. *Int J Cancer* **115**, 998–1005 (2005).
428 18. Meijer, D. H., Maguire, C. A., LeRoy, S. G. & Sena-Esteves, M. Controlling brain tumor growth by
429 intraventricular administration of an AAV vector encoding IFN-beta. *Cancer Gene Ther* **16**, 664–671
430 (2009).

431 19. Yoshida, J., Mizuno, M., Nakahara, N. & Colosi, P. Antitumor Effect of an Adeno-associated Virus
432 Vector Containing the Human Interferon-β Gene on Experimental Intracranial Human Glioma. *Jpn J*
433 *Cancer Res* **93**, 223–228 (2002).
434 20. GuhaSarkar, D., Su, Q., Gao, G. & Sena-Esteves, M. Systemic AAV9-IFNβ gene delivery treats highly
435 invasive glioblastoma. *Neuro Oncol* **18**, 1508–1518 (2016).
436 21. Hu, A., Ding, M., Zhu, J., Liu, J.-Q., Pan, X., Ghoshal, K. & Bai, X.-F. Intra-Tumoral Delivery of IL-27
437 Using Adeno-Associated Virus Stimulates Anti-tumor Immunity and Enhances the Efficacy of
438 Immunotherapy. *Front Cell Dev Biol* **8**, 210 (2020).
439 22. von Roemeling, C. A., Patel, J. A., Carpenter, S. L., Yegorov, O., Yang, C., Bhatia, A., Doonan, B. P.,
440 Russell, R., Trivedi, V. S., Klippel, K., Ryu, D. H., Grippin, A., Futch, H. S., Ran, Y., Hoang-Minh, L. B.,
441 Weidert, F. L., Golde, T. E. & Mitchell, D. A. Adeno-associated virus delivered CXCL9 sensitizes
442 glioblastoma to anti-PD-1 immune checkpoint blockade. *Nat Commun* **15**, 5871 (2024).
443 23. Xu, X., Chen, W., Zhu, W., Chen, J., Ma, B., Ding, J., Wang, Z., Li, Y., Wang, Y. & Zhang, X. Adeno-
444 associated virus (AAV)-based gene therapy for glioblastoma. *Cancer Cell International* **21**, 76 (2021).
445 24. Schoen, S., Kilinc, M. S., Lee, H., Guo, Y., Degertekin, F. L., Woodworth, G. F. & Arvanitis, C. Towards
446 controlled drug delivery in brain tumors with microbubble-enhanced focused ultrasound. *Advanced*
447 *Drug Delivery Reviews* **180**, 114043 (2022).
448 25. Nabavizadeh, A., Narsinh, K., Kaufmann, T. J., Liu, H., Pouliopoulos, A. N., Prada, F., Agarwal, V.,
449 Ellingson, B. M., Sanvito, F., Everson, R. G., Meng, Y., Gandhi, D., Chang, S. M., Wen, P. Y., Ahluwalia,
450 M. S., Sul, N., Hadley, L., Leblang, S., Shah, B. R., Arvanitis, C. D., Burns, T. C., Moosa, S. &
451 Woodworth, G. F. Focused Ultrasound in Brain Tumors: Mechanisms, Imaging Guidance, and
452 Emerging Clinical Applications. *American Journal of Neuroradiology*
453 https://doi.org/10.3174/ajnr.A9126 (2025) doi:10.3174/ajnr.A9126.
454 26. Arvanitis, C. D., Askoxylakis, V., Guo, Y., Datta, M., Kloepper, J., Ferraro, G. B., Bernabeu, M. O.,
455 Fukumura, D., McDannold, N. & Jain, R. K. Mechanisms of enhanced drug delivery in brain

456 metastases with focused ultrasound-induced blood-tumor barrier disruption. *Proc Natl Acad Sci U S A*
457 **115**, E8717–E8726 (2018).
458 27. Curley, C. T., Mead, B. P., Negron, K., Kim, N., Garrison, W. J., Miller, G. W., Kingsmore, K. M., Thim, E.
459 A., Song, J., Munson, J. M., Klibanov, A. L., Suk, J. S., Hanes, J. & Price, R. J. Augmentation of brain
460 tumor interstitial flow via focused ultrasound promotes brain-penetrating nanoparticle dispersion
461 and transfection. *Science Advances* **6**, eaay1344 (2020).
462 28. Zhu, H., Allwin, C., Bassous, M. G. & Pouliopoulos, A. N. Focused ultrasound-mediated enhancement
463 of blood–brain barrier permeability for brain tumor treatment: a systematic review of clinical trials. *J*
464 *Neurooncol* **170**, 235–252 (2024).
465 29. Kofoed, R. H., Dibia, C. L., Noseworthy, K., Xhima, K., Vacaresse, N., Hynynen, K. & Aubert, I. Efficacy
466 of gene delivery to the brain using AAV and ultrasound depends on serotypes and brain areas.
467 *Journal of Controlled Release* **351**, 667–680 (2022).
468 30. Thévenot, E., Jordão, J. F., O'Reilly, M. A., Markham, K., Weng, Y.-Q., Foust, K. D., Kaspar, B. K.,
469 Hynynen, K. & Aubert, I. Targeted delivery of self-complementary adeno-associated virus serotype 9
470 to the brain, using magnetic resonance imaging-guided focused ultrasound. *Hum Gene Ther* **23**,
471 1144–1155 (2012).
472 31. Alonso, A., Reinz, E., Leuchs, B., Kleinschmidt, J., Fatar, M., Geers, B., Lentacker, I., Hennerici, M. G.,
473 Smedt, S. C. de & Meairs, S. Focal Delivery of AAV2/1-transgenes Into the Rat Brain by Localized
474 Ultrasound-induced BBB Opening. *Molecular Therapy Nucleic Acids* **2**, (2013).
475 32. Hsu, P.-H., Wei, K.-C., Huang, C.-Y., Wen, C.-J., Yen, T.-C., Liu, C.-L., Lin, Y.-T., Chen, J.-C., Shen, C.-R. &
476 Liu, H.-L. Noninvasive and Targeted Gene Delivery into the Brain Using Microbubble-Facilitated
477 Focused Ultrasound. *PLOS ONE* **8**, e57682 (2013).
478 33. Kofoed, R. H., Heinen, S., Silburt, J., Dubey, S., Dibia, C. L., Maes, M., Simpson, E. M., Hynynen, K. &
479 Aubert, I. Transgene distribution and immune response after ultrasound delivery of rAAV9 and PHP.B
480 to the brain in a mouse model of amyloidosis. *Molecular Therapy Methods & Clinical Development*
481 **23**, 390–405 (2021).

482 34. Wang, S., Kugelman, T., Buch, A., Herman, M., Han, Y., Karakatsani, M. E., Hussaini, S. A., Duff, K. &
483 Konofagou, E. E. Non-invasive, Focused Ultrasound-Facilitated Gene Delivery for Optogenetics. *Sci*
484 *Rep* **7**, 39955 (2017).
485 35. Weber-Adrian, D., Thévenot, E., O'Reilly, M. A., Oakden, W., Akens, M. K., Ellens, N., Markham-
486 Coultes, K., Burgess, A., Finkelstein, J., Yee, A. J. M., Whyne, C. M., Foust, K. D., Kaspar, B. K., Stanisz,
487 G. J., Chopra, R., Hynynen, K. & Aubert, I. Gene delivery to the spinal cord using MRI-guided focused
488 ultrasound. *Gene Ther* **22**, 568–577 (2015).
489 36. Wang, S., Olumolade, O. O., Sun, T., Samiotaki, G. & Konofagou, E. E. Noninvasive, neuron-specific
490 gene therapy can be facilitated by focused ultrasound and recombinant adeno-associated virus. *Gene*
491 *Ther* **22**, 104–110 (2015).
492 37. Weber-Adrian, D., Kofoed, R. H., Chan, J. W. Y., Silburt, J., Noroozian, Z., Kügler, S., Hynynen, K. &
493 Aubert, I. Strategy to enhance transgene expression in proximity of amyloid plaques in a mouse
494 model of Alzheimer's disease. *Theranostics* **9**, 8127–8137 (2019).
495 38. Xhima, K., Nabbouh, F., Hynynen, K., Aubert, I. & Tandon, A. Noninvasive delivery of an α-synuclein
496 gene silencing vector with magnetic resonance–guided focused ultrasound. *Movement Disorders* **33**,
497 1567–1579 (2018).
498 39. Foiret, J., Zhang, H., Fite, B. Z., Ilovitsh, T., Mahakian, L. M., Tam, S., Beitnere, U., Pyles, B., Segal, D. J.
499 & Ferrara, K. W. Blood-brain barrier disruption for the delivery of non-infectious viral vectors and
500 proteins, preliminary study. in *2017 IEEE International Ultrasonics Symposium (IUS)* 1–4 (2017).
501 doi:10.1109/ULTSYM.2017.8092207.
502 40. Stavarache, M. A., Petersen, N., Jurgens, E. M., Milstein, E. R., Rosenfeld, Z. B., Ballon, D. J. & Kaplitt,
503 M. G. Safe and stable noninvasive focal gene delivery to the mammalian brain following focused
504 ultrasound. *Journal of Neurosurgery* **130**, 989–998 (2018).
505 41. Weber-Adrian, D., Kofoed, R. H., Silburt, J., Noroozian, Z., Shah, K., Burgess, A., Rideout, S., Kügler, S.,
506 Hynynen, K. & Aubert, I. Systemic AAV6-synapsin-GFP administration results in lower liver

507 biodistribution, compared to AAV1&2 and AAV9, with neuronal expression following ultrasound-
508 mediated brain delivery. *Sci Rep* **11**, 1934 (2021).
509 42. Todd, N., Owusu-Yaw, B., Fletcher, S.-M. P., Zhang, Y., McDannold, N. & Kegel-Gleason, K.
510 Comparison of gadolinium and AAV9-GFP distributions in the brain following focused ultrasound-
511 mediated delivery across the BBB. *Phys. Med. Biol.* **71**, 015014 (2025).
512 43. Ajenjo, J., Seo, J. W., Foiret, J., Wu, B., Raie, M. N., Wang, J., Fite, B. Z., Zhang, N., Malek, R., Beinat,
513 C., Malik, N., Anders, D. A. & Ferrara, K. W. PET imaging of focused-ultrasound enhanced delivery of
514 AAVs into the murine brain. *Theranostics* **13**, 5151–5169 (2023).
515 44. Arvanitis, C. D., Livingstone, M. S., Vykhodtseva, N. & McDannold, N. Controlled Ultrasound-Induced
516 Blood-Brain Barrier Disruption Using Passive Acoustic Emissions Monitoring. *PLOS ONE* **7**, e45783
517 (2012).
518 45. Foust, K. D., Nurre, E., Montgomery, C. L., Hernandez, A., Chan, C. M. & Kaspar, B. K. Intravascular
519 AAV9 preferentially targets neonatal neurons and adult astrocytes. *Nat Biotechnol* **27**, 59–65 (2009).
520 46. Seo, J. W., Ingham, E. S., Mahakian, L., Tumbale, S., Wu, B., Aghevlian, S., Shams, S., Baikoghli, M.,
521 Jain, P., Ding, X., Goeden, N., Dobreva, T., Flytzanis, N. C., Chavez, M., Singhal, K., Leib, R., James, M.
522 L., Segal, D. J., Cheng, R. H., Silva, E. A., Gradinaru, V. & Ferrara, K. W. Positron emission tomography
523 imaging of novel AAV capsids maps rapid brain accumulation. *Nat Commun* **11**, 2102 (2020).
524 47. Lee, H., Guo, Y., Ross, J. L., Schoen, S., Degertekin, F. L. & Arvanitis, C. Spatially targeted brain cancer
525 immunotherapy with closed-loop controlled focused ultrasound and immune checkpoint blockade.
526 *Sci Adv* **8**, eadd2288 (2022).
527 48. Sun, T., Zhang, Y., Power, C., Alexander, P. M., Sutton, J. T., Aryal, M., Vykhodtseva, N., Miller, E. L. &
528 McDannold, N. J. Closed-loop control of targeted ultrasound drug delivery across the blood–
529 brain/tumor barriers in a rat glioma model. *PNAS* **114**, E10281–E10290 (2017).
530 49. Patel, A., Schoen, S. J. & Arvanitis, C. D. Closed-Loop Spatial and Temporal Control of Cavitation
531 Activity With Passive Acoustic Mapping. *IEEE Transactions on Biomedical Engineering* **66**, 2022–2031
532 (2019).

533 50. Reul, J., Frisch, J., Engeland, C. E., Thalheimer, F. B., Hartmann, J., Ungerechts, G. & Buchholz, C. J.
534 Tumor-Specific Delivery of Immune Checkpoint Inhibitors by Engineered AAV Vectors. *Front Oncol* **9**,
535 52 (2019).
536 51. Grifman, M., Trepel, M., Speece, P., Gilbert, L. B., Arap, W., Pasqualini, R. & Weitzman, M. D.
537 Incorporation of tumor-targeting peptides into recombinant adeno-associated virus capsids. *Mol*
538 *Ther* **3**, 964–975 (2001).
539 52. Shen, S., Berry, G. E., Castellanos Rivera, R. M., Cheung, R. Y., Troupes, A. N., Brown, S. M., Kafri, T. &
540 Asokan, A. Functional analysis of the putative integrin recognition motif on adeno-associated virus 9.
541 *J Biol Chem* **290**, 1496–1504 (2015).
542 53. Cheng, B., Ling, C., Dai, Y., Lu, Y., Glushakova, L. G., Gee, S. W. Y., McGoogan, K. E., Aslanidi, G. V.,
543 Park, M., Stacpoole, P. W., Siemann, D., Liu, C., Srivastava, A. & Ling, C. Development of optimized
544 AAV3 serotype vectors: mechanism of high-efficiency transduction of human liver cancer cells. *Gene*
545 *Ther* **19**, 375–384 (2012).
546 54. Arvanitis, C. D., Crake, C., McDannold, N. & Clement, G. T. Passive Acoustic Mapping with the Angular
547 Spectrum Method. *IEEE Transactions on Medical Imaging* **36**, 983–993 (2017).

548